TIME RESOLVED SPECTROSCOPY OF A LEONID FIREBALL AFTERGLOW

JIŘÍ BOROVIČKA
Astronomical Institute, Ondřejov Observatory, 251 65 Ondřejov, Czech Republic
E-mail: borovic@asu.cas.cz

PETER JENNISKENS
SETI Institute, NASA ARC, Mail Stop 239-4, Moffett Field, CA 94035-1000, USA
E-mail: pjenniskens@mail.arc.nasa.gov

(Received 7 July 2000; Accepted 31 July 2000)

Abstract. Two video spectra of a meteoric afterglow were obtained for the first time during the 1999 Leonid aircraft campaign. The train was produced by a -13 magnitude Leonid fireball at a relatively low height between 91–75 km. The meteor spectrum has a strong hydrogen emission, proportional to 10-20 H atoms per one Fe atom The train spectrum consisted of a red continuum, yellow continuum, and about 50 atomic lines between 3700–9000 Å. The yellow continuum, possibly due to NO_2, was also detected in the persistent train. The red continuum is interpreted as a thermal radiation of dust from meteoric debris at about 1400 K. Evidence for secondary ablation is found in the afterglow. The atomic lines decayed within seconds of the meteor. The lines of Fe I, Mg I, Na I, Ca I, Ca II, Cr I, Mn I, K I, and possibly Al I were present in the glow together with the 5577 Å forbidden O I line. The gas temperature in the train was close to 5000 K at the beginning and decayed to 1200 K within two seconds. However, thermal equilibrium was not satisfied for all populated levels.

Keywords: Afterglow, debris, dust, *H*, meteor, persistent train, spectroscopy

1. Introduction

On November 18, 1999 at 04$^{\mathrm{h}}$00$^{\mathrm{m}}$29$^{\mathrm{s}}$ UT, about two hours after the maximum of the 1999 Leonid meteor storm, a very bright Leonid meteor appeared over the island of Corse, France, and produced an afterglow evolving into a persistent train that was visible to the naked eye for several minutes. The meteor and the glow were observed by several instruments on-board two aircrafts flying above the Mediterranean during the 1999 Leonid Multi-Instrument Aircraft Campaign (Jenniskens *et al.*, 2000). For the first time, spectra of the afterglow were captured by video spectrographs. These data provide information about the physical conditions in the path of the meteor just after the train formation. A low resolution spectrum of the persistent train at later stages was obtained with the same instrument as well.

The spectra were obtained by two spectrographs of similar construction, the Ondřejov spectrograph assembled at the Ondřejov Observa-

Table I.

	Ondřejov spectrograph	BETSY spectrograph
image intensifier	Dedal 41	Mullard XX1332
camcorder	Panasonic NV-S88E	Sony CCD-TRV69E
video format	S-VHS, PAL	Hi-8, PAL
frames per second	25	25
lens diameter	36 mm	140 mm
focal length	50 mm	105 mm
grating diameter	52 mm	140 mm
grating grooves density	600 mm^{-1}	230 mm^{-1}
first order dispersion	11 Å pixel^{-1}	16 Å pixel^{-1}
field of view	25°	20 °
aircraft	FISTA	FISTA
window elevation	12°	62°
camera elevation	35°	62°

tory and the BETSY spectrograph assembled at the SETI Institute. Both instruments consist basically of an optical sequence of transmission grating, lens, image intensifier, and video camcorder. The actual system parameters are given in Table I. The spectrographs are slitless, so the given dispersion is valid when imaging a narrow object. For objects with significant angular width, the spectral resolution will be worse.

The spectrographs were placed on-board the FISTA aircraft and directed to different positions on the sky. The fireball occurred outside the fields of view, but, fortunately, the gratings were in such positions that high order spectra of the terminal parts of the fireball and of the afterglow fell within the fields of view of both instruments. As the train weakened, its spectrum ceased to be visible in the high orders after about five seconds. After that, the Ondřejov spectrograph was moved manually with the aim to capture the first order spectrum of the persistent train. Due to a difficult orientation from the airplane, this succeeded for only a short period of time 37 seconds after the train formation and, finally, from 1 minute 23 seconds after the train formation.

The fireball itself was imaged by a direct non-spectral image intensified camera on-board the other aircraft, called ARIA, 160 km south of FISTA. The combination of observations from both aircrafts enabled us to determine the fireball trajectory.

Table II.

	beginning	maximum light	end
relative time [s]	0.00	1.77	2.17
longitude [East]	9°.57	8°.93	8°.78
latitude [North]	41°.51	41°.83	41°.90
altitude [km]	191	82	56
absolute magnitude	+2	< -10	0
distance to ARIA [km]	354	303	298
distance to FISTA [km]	—	203	191
elevation at ARIA	29°	12°	7°
elevation at FISTA	—	19°	13°
velocity [km/s]	72	72	(60)
geocentric radiant	$\alpha = 153°.3$, $\delta = +21°.2$, ±2° Az = 303°, $h = 59°$		

In this paper we present all available data and their basic interpretation. The trajectory, light curve and spectrum of the mother fireball are given first. Then the structure of the afterglow and its spectrum are described, including detailed identification of spectral lines. The intensities and intensity decay rates of important lines are given and a very simple model is used to derive the temperature decay in the train during the first seconds. The spectrum of the persistent train at later times is discussed. Finally, our data are compared to the spectra of meteor trains obtained by other authors.

2. Fireball trajectory and light curve

At 04:00:29 UT, when the fireball occurred, the position of the aircrafts, as measured by the GPS system, was 7°11′15″ E, 40°45′05″ N, 1230 m altitude for FISTA and 7°03′44″ E, 39°36′19″ N, 1253 m for ARIA. Since no direct image of the fireball from FISTA exists, we used the spectrum from the Ondřejov spectrograph to derive the position of the fireball. The extrapolation introduces some uncertainty into the fireball trajectory computation, nevertheless, we were able to obtain quite consistent results. The consistency of the geometry was confirmed by the fact that the computed fireball velocity was close to 72 km s^{-1} when using measurements from either aircraft, and that the altitudes of the fireball terminal point and of the lower end of the train agreed

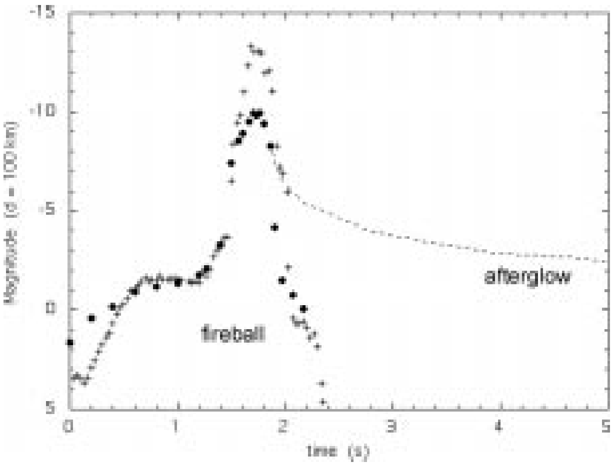

Figure 1. Lightcurve of the fireball and the train measured on the ARIA camera data (●). Since the camera was saturated, the real maximum brightness was certainly higher. An independent assessment (Jenniskens & Rairden 2000) yielded a value of −13 mag (+).

to within several hundreds of meters. We, therefore, conclude that the precision of the derived altitudes is better than 1 km. The final data on fireball trajectory are given in Table II. Indeed, there is good agreement with the independent trajectory calculations by Jenniskens & Rairden (2000), who derived the FISTA fireball position from back tracking the persistent train.

The fact that the fireball lasted for 2.17 sec while the Leonid radiant was 60 degrees above horizon means that the altitude span must have been about 135 km. The beginning altitude was found to be 191 km, with hint that the meteor was visible even a few kilometers higher. This high beginning is consistent with the observations of bright Leonids by Spurný *et al.* (2000a). Above the altitude of 140 km, the meteor had the same diffuse appearance as described by Spurný *et al.* (2000b). Between 90–75 km the fireball exhibited bright flare, evidently caused by a disintegration of the meteoroid. Nevertheless, part of the meteoroid survived and disappeared only at the altitude of 56 km, which is probably a record low altitude for a Leonid. A −13 mag Leonid 98023 of Spurný *et al.* (2000a,b) had a similar behavior with bright outburst and a surviving remnant continuing down, but the outburst terminated at 82 km and the remnant disappeared at 73 km. Another −13 mag Leonid 98041 terminated the burst at 73 km, similarly to the present fireball but there was no surviving fragment.

The approximate light curve is given in Figure 1. where we included the intensity decay of the afterglow. The magnitude

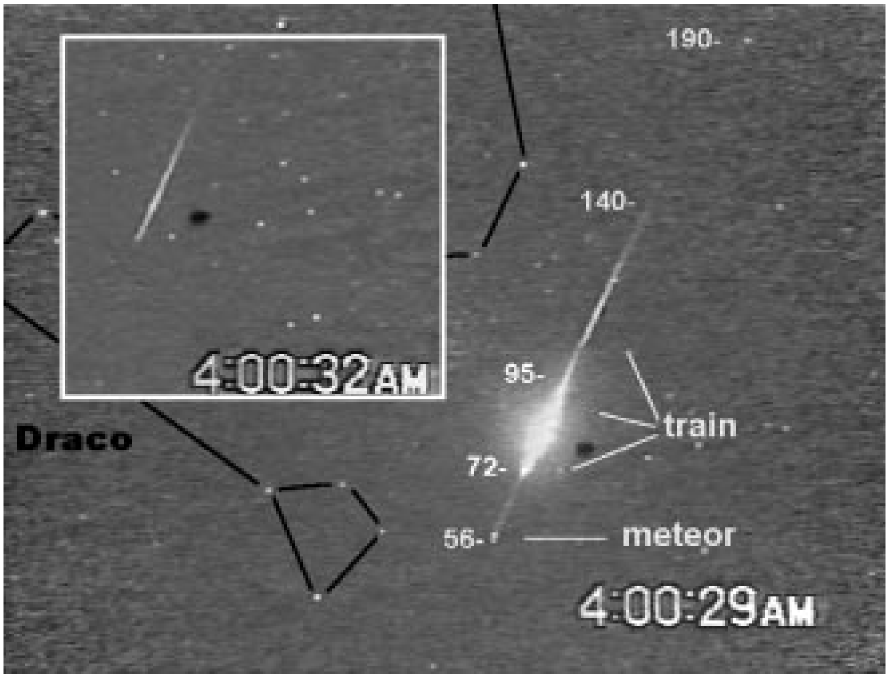

Figure 2. A single frame, including the original time stamp, taken by the direct image camera from the ARIA aircraft. The meteor just before its disappearance and the bright train above it can be seen. The numbers mark altitudes in km. The position of the constellation of Draco is indicated. The inset figure shows the train three seconds later. The inset is an average of nine frames.

given in absolute scale, i.e. recomputed to 100 km distance. The actual distance from ARIA was nearly 300 km (see Table II). Due to camera saturation, the meteor peak brightness could not be well determined and the measured value of −13 mag is somewhat uncertain. The photometric mass of the meteoroid is about 1 kg.

In Figure 2, the meteor just before its disappearance and the bright afterglow left behind the meteor are shown in a single video frame from the ARIA camera. The bright afterglow lies at the position where the meteor flared a fraction of second earlier. Fainter afterglow continue up to the altitude of 140 km. The initial total brightness of the train was about −8 mag (see Figure 1).

3. Fireball Spectrum

The information on the fireball spectrum is limited. During the flare, the spectrum was mostly saturated, although BETSY has useful records of the reflected spectrum from the aircraft window (see Figure 3).

Table III.

Line		eV	S.
3829.4–38.3	Mg I 3	5.9	1
3859.9	Fe I 4	3.2	1
3933.7	Ca II 1	3.2	6
3968.5	Ca II 1	3.1	6
4226.7	Ca I 2	2.9	2
4375.9)	Fe I 2	2.8	2
4383.6)	Fe I 41	4.3	
4404.8	Fe I 41	4.4	1
4427.3	Fe I 2	2.9	1
4481.2	Mg II 4	11.6	4
4558.7	Cr II 44	6.8	1
4583.8	Fe II 38	5.5	1
4630.5	N II 5	21.2	2
4703.0	Mg I 11	7.0	1
4861.3	H β	12.7	3
4871.3–72.1	Fe I 318	5.4	1
4890.8–91.5	Fe I 318	5.4	1
4919.0–20.5	Fe I 318	5.4	2
4923.9	Fe II 42	5.4	3
4957.3–57.6	Fe I 318	5.3	2
5005.2	N II 19	23.1	3
5018.4	Fe II 42	5.4	3
5056.0	Si II 5	12.5	2
5110.4	Fe I 1	2.4	2
5167.3–83.6)	Mg I 2	5.1	4
5169.0)	Fe II 42	5.3	
5204.5–08.4	Cr I 7	3.3	1
5227.2	Fe I 37	3.9	2
5269.5)	Fe I 15	3.2	3
5270.4)	Fe I 37	4.0	
5328.0)	Fe I 15	3.2	2
5329.1–30.7)	O I 12	13.1	
5371.5	Fe I 15	3.3	2
5397.1–05.8	Fe I 15	3.2	2
5429.7–34.5	Fe I 15	3.3	2
5446.9–55.6	Fe I 15	3.3	2
5497.5–06.8	Fe I 15	3.2	1
5528.4	Mg I 9	6.7	1
5577.3	O I 3F	4.2	2
5615.6)	Fe I 686	5.5	1
5616.5)	N I 24	14.0	
5666.6–79.6	N II 3	20.6	2
5890.0–95.9	Na I 1	2.1	5
6156.0–58.2	O I 10	12.8	3
6347.1	Si II 2	10.1	5
6371.4	Si II 2	10.1	4
6562.8	H α	12.1	5
7423.6	N I 3	12.0	4
7442.3	N I 3	12.0	5
7468.3	N I 3	12.0	5
7771.9–75.4	O I 1	10.7	6
8184.8–88.0	N I 2	11.8	3
8216.3–23.1	N I 2	11.8	5
8242.5	N I 2	11.8	2
8446.3–46.8	O I 4	11.0	4
8498.0	Ca II 2	3.2	2
8542.1	Ca II 2	3.2	6
8629.2	N I 8	12.1	2
8662.1	Ca II 2	3.1	5
8680.2–83.4	N I 1	11.8	4
8711.7	N I 1	11.8	2

Before the flare, part of the spectrum is present on the BETSY spectrograph, while the spectrum was out of field of view on the Ondřejov spectrograph. The surviving remnant was well placed for both spectrographs but it was not very bright.

The combination of the data yielded the list of atomic lines present in the spectrum of the fireball (Table III). The excitation potential of the upper level is given for each transition. Unresolved lines are joined by parentheses. The relative strength of the lines is given on a scale from 1 to 6, the lines marked by 6 being the strongest. We refrain from a more meaningful intensity measure at this point because the spectrum changed along the trajectory.

All atomic lines in Table III have previously been found in photographic spectra of high velocity fireballs – see the detailed list of Halliday (1961). This is the reason why we do not give more details about the identification procedure for the fireball spectrum, in contrast to the afterglow spectrum in the next sections. In fact, a photographic spectrum of a fireball of this brightness would be superior to our video spectra and would undoubtedly yield much more line identifications.

From Table III it can be seen, that lines of very different excitation+ionization energy are present: from 2 eV for Na I lines to about 35 eV needed to ionize and excite nitrogen atoms to produce the N II lines. In addition, lines of different origin are present: nitrogen and a substantial part of oxygen come from the atmosphere, while other elements come from the meteoroid. This assignment follows from comparing relative abundances of elements in the radiating gas and also from the behavior of individual emissions along the trajectory.

We can therefore divide the lines in several groups or components according to their origin and energy, following partly Borovička (1994) and Borovička and Boček (1995):

		origin	
		atmospheric	meteoric
energy	low	[O I] 5577 Å	Na I, Mg I, Fe I, Ca I, Cr I, Ca II
	high	O I, N I	Ca II, Mg II, Si II, H I, Fe II, Cr II
	very high	N II	*none*

The low energy meteoric group is identical to Borovička's (1994) main component of temperature of about 5000 K and the high energy meteoric group corresponds to the second component of about 10,000 K. The temperatures of the atmospheric lines are difficult to establish.

The relative strength of individual groups of lines changed along the meteor trajectory. We have no information about the meteor spectrum at high altitudes above 110 km. Before the flare, at about 100 km, the spectrum was dominated by the atmospheric lines of O I and N I. As the brightness increased, the low energy meteoric lines become strong. At the peak brightness, in the flare, the high energy meteoric lines dominated the spectrum and the N II lines were also present. In the spectrum of the surviving remnant, the O I and N I lines were the brightest again, but the low and high energy meteoric lines were also present.

The changes of the spectrum are intriguing. For example, the 8500 Å region is dominated by the N I and O I lines before and after the flare and the Ca II lines are hardly visible. In the flare, on the other hand, the Ca II lines are extremely bright, in fact the brightest lines in the whole spectrum.

A detailed explanation of the above facts is not the scope of the present paper. The general picture seems, however, to be clear. The flare was caused by dramatic fragmentation and violent evaporation of the meteoroid. The amount of the meteoric vapors increased rapidly and the intensity of meteoric lines therefore increased much more than the intensity of the atmospheric lines. The lines of the second meteoric component brightened more than the lines of the main component because the second component is optically thin (Borovička and Majden 1998). It seems that the development of the second component was accompanied with the atmospheric lines of N II. These emissions are probably connected with the development of meteor shock wave, while the main component and the O I and N I lines are present also in the absence of shock wave at higher altitudes. At low altitudes, the shock wave is present also in the absence of a meteor flare. It is interesting that the atmospheric lines in both cases fall to higher energy groups than the related meteoric lines. The correlation of the brightenings of Si II and N II lines was found also in the spectrum of the Benešov fireball (Borovička and Spurný 1996).

The presence of N II lines in meteor spectra was first found by Halliday (1961). Their excitation energy by far exceeds other lines in the spectrum, nevertheless, it is still only a fraction of the kinetic energy of N_2 molecule at 72 km s^{-1} (750 eV). O II lines of atmospheric origin can be expected in the spectrum as well but O II lines are fainter than N II and their presence could not be firmly confirmed.

Of special interest are the hydrogen lines since they may suggest the presence of organic matter in the meteoroid. H α and H β are well seen in the flares and in the surviving remnant spectrum. Their presence is not surprising, H lines have been seen e.g. in Perseid spectra (first found by Millman 1953). However, they are brighter in the present spectrum. Assuming the temperature of 10,000 K for the second component the ratio of number of atoms H/Fe $\approx$ 10–20 was found, while the values for Perseids are 2–6 (Borovička and Betlem 1997).

4. The spatial structure of the afterglow

The image of the afterglow in Figure 2 has a low resolution. The structure of the bright part of the glow can be better seen on the spectrograph records. In Figure 3 it can be seen that the glow after its formation consisted of four segments, which we numbered 1 to 4. The segments are separated by gaps with almost no emission (except for the 5577 Å line). The uppermost segment 1 is the brightest, longest and has a sharp leading edge. The lower segments are fainter, shorter and more symmetrical. The reality of the structure is confirmed on the image from the Ondřejov spectrograph in Figure 4. Here the altitude scale is also drawn. Segment 1 goes from about 85 km to 80 km, the center of segment 4 lies at 73 km. We believe that individual segments were formed at the positions of individual consecutive meteoroid break-ups and dust releases.

When playing the video, it was noted that the leading edge of the glow segment 1 moves down. The motion relative to a background star was evident as well as the fact that the gap between segments 1 and 2 became narrower. The movement was measured on the Ondřejov spectrograph data and the result is displayed in Figure 5. The train travelled 1.5 km within one second, with the initial velocity of about 2 km s^{-1}. This observation confirms that the train was formed by ablated material, dust and gas, which has its own inertia and continued the motion through (probably rarified) air in the track of the main body.

5. Afterglow spectrum, line identifications

The spectrum of the afterglow consists of numerous lines and a continuous radiation. Figures 3 and 4 show that the spectra of all glow segments are nearly the same and contain different lines than the meteor spectrum. The BETSY spectrum (Figure 3) is well placed on the diagonal of the frame, however, it is an overlap of five different spectral orders (3rd to 7th) which makes the line identification difficult. The Ondřejov spectrum consists of the red part of the unblazed first order spectrum and a part of the second order spectrum. The wavelength scale is shown in Figure 4. The system is sensitive in the range 3800–9000 Å but there is no information on the interval 6000–7000 Å. For the brightest segment 1, an even smaller part of the spectrum lies in the field of view. About 2.5 seconds after the fireball the camera was slightly moved, so the segment 1 moved nearly to the position of the meteor in Figure 4 and the whole wavelength range was accessible. At that time, however, only four lines remained visible. Later, the grating

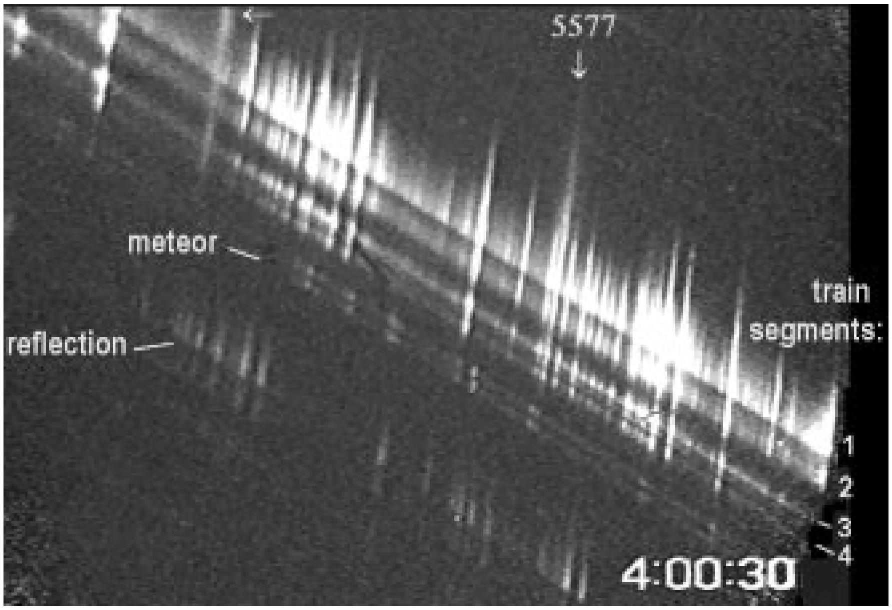

Figure 3. A single frame taken by the BETSY spectrograph. High order spectra of the meteor and the afterglow can be seen. Four separate train segments are numbered. An internal reflection of the bright part of the glow spectrum is also present. The position of the green oxygen line at 5577 Å (in the 4rd and 5th order) is marked by arrows. The camera time was not quite synchronized with the ARIA camera (Figure 2).

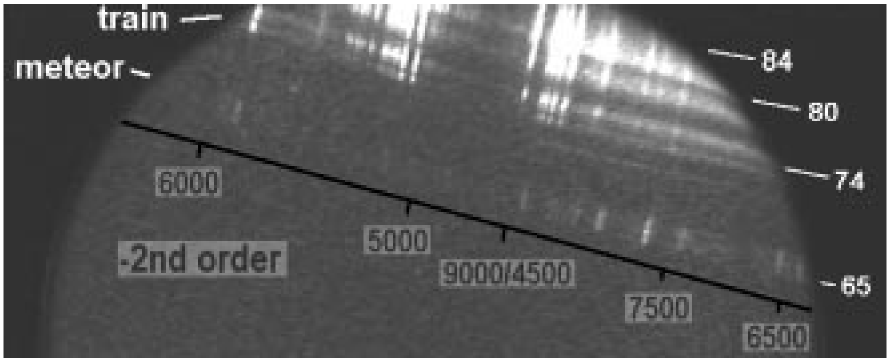

Figure 4. Upper part of a single frame taken by the Ondřejov spectrograph with circular field of view. Meteor and afterglow spectrum can be seen. The white numbers mark altitudes in km, the dark numbers show approximate wavelengths in Å. The end of the −1st order and the beginning of the −2nd order overlap.

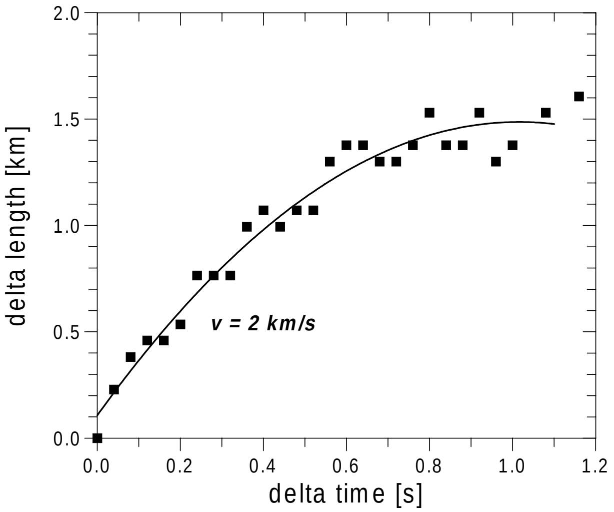

Figure 5. The displacement of the leading edge of glow segment 1 as a function of time after the segment formation. A parabolic fit is drawn through the measured points.

was rotated by 180 degrees and the blazed first order spectrum was searched for persistent train emissions. This succeeded only 1 minute 23 seconds after the train formation. The inspection of the tape revealed, that the first order spectrum appeared in the field of view for a short period of time also at 37 s. At both these times the train spectrum consisted only of a continuos radiation as shown in Figure 6.

Most of this paper is devoted to an analysis of the first 2–3 seconds of the afterglow, when we have a plenty of information from the atomic lines. The persistent train at later times is discussed in Section 8.

As an example, the plot of the spectrum of glow segment 3 is presented in Figure 7. Besides the lines, strong continuum is also present in the glow spectrum. We divided the continuum into two parts which have probably different origins, the red continuum observed in the first order and a yellow continuum seen in the second order (see Figure 7). The red continuum could be fitted relatively well with a blackbody of the temperature of about 1400 K and we attribute it tentatively to a thermal radiation of dust. The yellow continuum is probably due to molecular emissions. Possible identifications will be discussed in Sect. 8.

The identification of the atomic lines was done in several steps. First, an an approximate wavelength scale was determined by using the lines in the meteor spectrum. The identification of the brightest lines of Na and Fe then became immediately clear. Other lines were identified after revising the wavelength scale and some faint lines could be identified only after the physical conditions in the train were considered (Sect. 7).

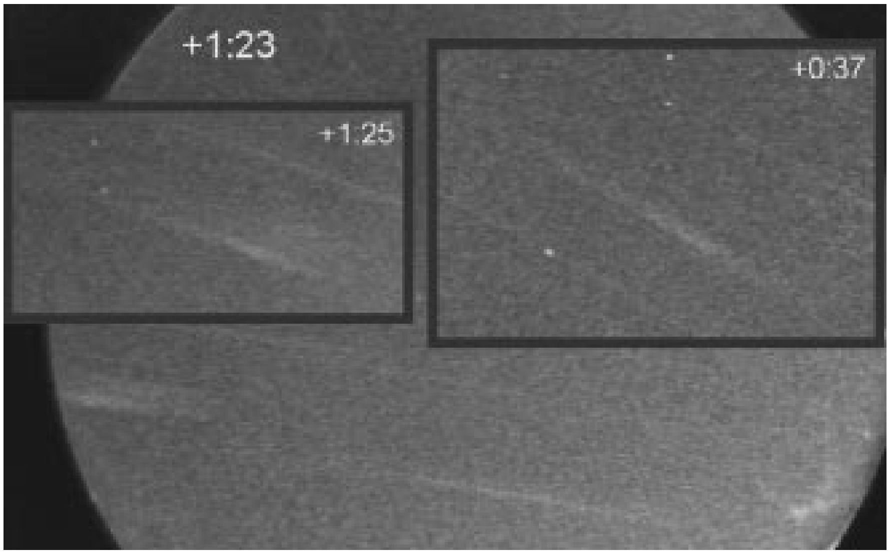

Figure 6. First order spectra of the persistent train. The background image shows the train (zero order) at lower right and a part of its spectrum on the left 1 minute and 23 seconds after the train formation. The insets show whole train spectra at different times.

In all cases the presence of the line in the spectra of both spectrographs and in different spectral orders was checked. The final identifications for the Ondřejov spectrum are given in Table IV and for the BETSY spectrum in Tables V–VIII.

The arrangement of both tables is similar. The visually estimated intensity of the line is given on scale 1–5. The observed intensity is affected by the wavelength dependent sensitivity in different spectral orders. The observed wavelengths are ambiguous in most cases and are given for all possible orders. The identification contains the laboratory wavelength, atom, ionization degree, and multiplet number according to multiplet table (Moore 1945).

With the exception of the oxygen green line 5577 Å, the afterglow spectrum contains only lines of ablated metals. Lines of neutral Fe, Mg, Na, Ca, Cr, Mn, and K and ionized Ca are present. The lines of Fe are the most numerous. The presence of Al is not certain. The identification of the K I line at 7699 Å seemed doubtful, because there is an alternative explanation of this line by the Fe I 3859 Å line in the second order and another K line at 7664 Å, which should be brighter, is very faint. However, the 7664 Å line is absorbed by the underlying atmospheric O_2 and we concluded that the 7699 Å line really is the main contributor to the observed feature. The only ionic lines present belong to Ca II. Calcium is the only abundant element with relatively

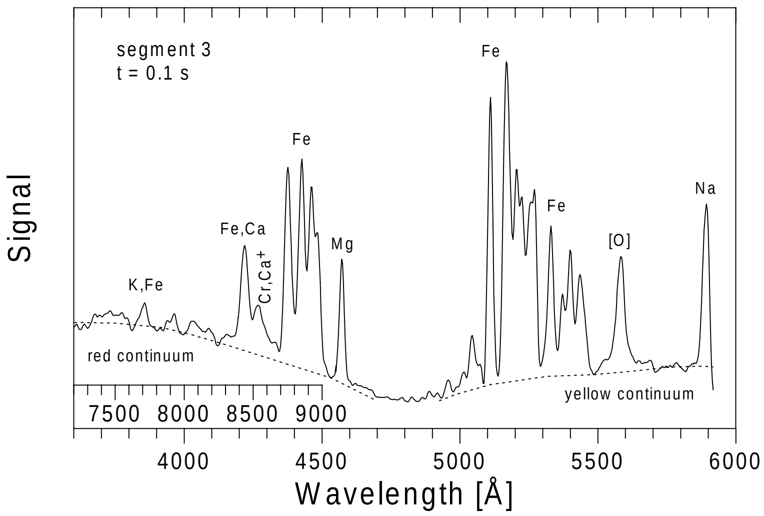

Figure 7. The wavelength calibrated spectrum of the afterglow segment 3 0.1 s after its formation extracted from the Ondřejov spectrograph. The lower wavelength scale corresponds to the second order, the upper scale is for the first order. In the overlapping region the wavelengths are ambiguous. Important lines are identified. The brightness of the Na line is underestimated because this line lies at the edge of the field of view.

low ionization potential (6.1 eV) and strong low excitation (3.1 eV) ionic lines. The excitation potential of all lines in the train is up to 7 eV. The high excitation potential of the allowed transitions of O and N is probably the reason why these lines are not present.

The strongest lines are the multiplets 1 and 2 of Fe I and multiplets 1 of Na I and Ca I. All have low excitation potential but they differ in transition probability. The Na line is a strong allowed transition, while the other lines are semi-forbidden intercombination transitions which are normally relatively faint. The explanation of their strength in the train is given in Sect. 7.

The forbidden green oxygen line has an evidently different origin than other lines. This line forms a short-living train in all Leonids and other fast meteors, even in faint ones. In our case the green line does not follow the structure of the glow segments, but dominates the upper part of the train up to the altitude of 140 km. The intensity of the green line is therefore not related to the ablation rate, which is consistent with the atmospheric origin of the line.

Table IV.

No	Int.	Wavelength		Identifications
		−1	−2	
1	1	7430	3715	3719.9 Fe I 5
2	1	7670	3835	7664.9 K I 1
3	3	7710	3855	3859.9 Fe I 4 7699.0 K I 1
4	2	7880	3940	3944.0 Al I 1 3930.3 Fe I 4 3927.9 Fe I 4 3933.7 Ca II 1
5	3	7930	3965	3961.5 Al I 1 7912.9 Fe I 12
6	3	8060	4030	4030.8 Mn I 2 4033.1 Mn I 2 4034.5 Mn I 2 4045.8 Fe I 43 8047.6 Fe I 12 8075.1 Fe I 12
7	2	8200	4100	8194.8 Na I 4 8183.5 Na I 4
8	2	8290	4145	4134.3 Fe I 3 4143.9 Fe I 43 4152.2 Fe I 18
9	1	8360	4180	4177.6 Fe I 18 4174.9 Fe I 19 4172.7 Fe I 19
10	4	8440	4220	4216.2 Fe I 3 4226.7 Ca I 2 4206.7 Fe I 3
11	3	8540	4270	4274.8 Cr I 1 8542.0 Ca II 2
12	2	8580	4290	4291.5 Fe I 3 4289.7 Cr I 1
13	2	8660	4330	8662.1 Ca II 2
14	5		4377	4375.9 Fe I 2
15	5		4428	4427.3 Fe I 2
16	4		4463	4461.7 Fe I 2
17	4		4483	4482.2 Fe I 2 4489.7 Fe I 2
18	4		4570	4571.1 Mg I 1
19	2		4651	4646.2 Cr I 21 4652.2 Cr I 21
20	2		4706	4703.0 Mg I 11
21	2		4870	4871.3 Fe I 318
22	2		4892	4891.5 Fe I 318 4890.8 Fe I 318
23	2		4918	4920.5 Fe I 318 4919.0 Fe I 318
24	2		4956	4957.6 Fe I 318 4957.3 Fe I 318
25	2		5012	5012.1 Fe I 16
26	3		5042	5041.8 Fe I 36
27	1		5072	5072.9 Cr I 8
28	5		5110	5110.4 Fe I 1
29	5		5168	5166.3 Fe I 1 5168.9 Fe I 1 5167.5 Fe I 37 5171.6 Fe I 36
30	4		5204	5204.6 Fe I 1 5208.4 Cr I 7 5206.0 Cr I 7 5204.5 Cr I 7
31	4		5227	5225.5 Fe I 1 5227.2 Fe I 37
32	4		5255	5255.0 Fe I 1 5250.2 Fe I 1 5247.0 Fe I 1
33	4		5269	5269.5 Fe I 15 5270.3 Fe I 37
34	4		5330	5328.0 Fe I 15
35	3		5370	5371.5 Fe I 15
36	3		5400	5405.8 Fe I 15 5397.1 Fe I 15 5394.7 Mn I 1
37	3		5435	5434.5 Fe I 15 5429.7 Fe I 15 5432.5 Mn I 1 5446.9 Fe I 15
38	2		5502	5501.5 Fe I 15 5506.8 Fe I 15 5497.5 Fe I 15
39	2		5528	5528.4 Mg I 9
40	4		5581	5577.3 O I 3F
41	5		5892	5890.0 Na I 1 5895.9 Na I 1
42	(5)		6570	6572.8 Ca I 1

Table V.

Line No.	Int.	Observed wavelength					Identifications
		−3	−4	−5	−6	−7	
1	4	6100	4575				4571.1 Mg I 1
2	2	6160	4620				6162.2 Ca I 3
3	2	6280	4710	3768			6280.6 Fe I 13 4703.0 Mg I 11
4	3	6361	4771	3817			6358.7 Fe I 13
5	2	6400	4800	3840			6400.3 Fe I 13
6	1	6440	4830	3864			3859.9 Fe I 4 6439.1 Ca I 18
7	2	6492	4869	3895			4871.3 Fe I 318 6498.9 Fe I 13
8	5	6565	4924	3939			6572.8 Ca I 1
9	3	6607	4955	3964			4957.6 Fe I 318 4957.3 Fe I 318 3961.5 Al I 1
10	2	6679	5009	4007			5012.1 Fe I 16
11	2	6723	5042	4034			5041.8 Fe I 36 4030.8 Mn I 2 4033.1 Mn I 2 4034.5 Mn I 2
12	2	6773	5080	4064			5072.9 Cr I 8 4063.6 Fe I 43
13	5	6812	5109	4087			5110.4 Fe I 1
14	5	6889	5167	4134			5166.3 Fe I 1 5168.9 Fe I 1 5167.5 Fe I 37 5171.6 Fe I 36
15	4	6941	5206	4165			5204.6 Fe I 1 5208.4 Cr I 7 5206.0 Cr I 7 5204.5 Cr I 7
16	4	6973	5230	4184			5225.5 Fe I 1 5227.2 Fe I 37
17	4	7013	5260	4208			5255.0 Fe I 1 5250.2 Fe I 1 5247.0 Fe I 1
18	4	7033	5275	4220			5269.5 Fe I 15 5270.3 Fe I 37 4216.2 Fe I 3 4226.7 Ca I 2
19	4	7111	5333	4266			5328.0 Fe I 15

Table VI.

Line No.	Int.	Observed wavelength					Identifications
		−3	−4	−5	−6	−7	
20	3	7163	5372	4298			5371.5 Fe I 15
21	3	7203	5402	4322			5405.8 Fe I 15 5397.1 Fe I 15 5394.7 Mn I 1
22	3	7247	5435	4348			5434.5 Fe I 15 5429.7 Fe I 15 5432.5 Mn I 1 5446.9 Fe I 15
23	4	7300	5475	4380			4375.9 Fe I 2
24	2	7340	5505	4404			5501.5 Fe I 15 5506.8 Fe I 15 5497.5 Fe I 15
25	4	7383	5537	4430			4427.3 Fe I 2
26	4	7437	5578	4462	3719		4461.7 Fe I 2 5577.3 O I 3F
27	4	7477	5608	4486	3739		4482.2 Fe I 2 4489.7 Fe I 2
28	4	7620	5715	4572	3810		4571.1 Mg I 1
29	1	7664	5748	4598	3832		7664.9 K I 1
30	2	7700	5775	4620	3850		3859.9 Fe I 4 7699.0 K I 1
31	1	7763	5822	4658	3881		4646.2 Cr I 21 4652.2 Cr I 21 3886.3 Fe I 4 3878.6 Fe I 4
32	5	7855	5891	4713	3927		5890.0 Na I 1 5895.9 Na I 1
33	3	7933	5950	4760	3967		3961.5 Al I 1 7912.9 Fe I 12 5956.7 Fe I 14 5949.3 Fe I 14 5958.2 Fe I 14
34	2	8047	6035	4828	4023		8047.6 Fe I 12 4030.8 Mn I 2
35	1	8083	6062	4850	4041		8075.1 Fe I 12
36	1	8140	6105	4884	4070		6102.7 Ca I 3 6122.2 Ca I 3 4891.5 Fe I 318 4890.8 Fe I 318

Table VII.

Line No.	Int.	Observed wavelength					Identifications
		−3	−4	−5	−6	−7	
37	2	8204	6153	4922	4102		4920.5 Fe I 318 4919.0 Fe I 318 6162.2 Ca I 3 8194.8 Na I 4 8183.5 Na I 4
38	1	8261	6196	4957	4131		4957.6 Fe I 318 4957.3 Fe I 318
39	1	8347	6260	5008	4173		6280.6 Fe I 13 5012.1 Fe I 16
40	2	8400	6300	5040	4200		5041.8 Fe I 36
41	3	8427	6320	5056	4213		4216.2 Fe I 3 4206.7 Fe I 3 4226.7 Ca I 2
42	5	8523	6392	5114	4261		5110.4 Fe I 1
43	5	8613	6460	5168	4307		5166.3 Fe I 1 5168.9 Fe I 1 5167.5 Fe I 37 5171.6 Fe I 36
44	4	8667	6500	5200	4333	3714	5204.6 Fe I 1 5208.4 Cr I 7 5206.0 Cr I 7 5204.5 Cr I 7
45	3	8707	6530	5224	4353	3731	5225.5 Fe I 1 5227.2 Fe I 37
46	5	8760	6570	5256	4380	3754	4375.9 Fe I 2 6572.8 Ca I 1
47	4	8849	6637	5310	4425	3793	4427.3 Fe I 2
48	2	8880	6660	5328	4440	3806	5328.0 Fe I 15
49	4	8920	6690	5352	4460	3823	4461.7 Fe I 2
50	4	8969	6727	5382	4485	3844	4482.2 Fe I 2 4489.7 Fe I 2 5371.5 Fe I 15
51	3	9000	6750	5400	4500	3857	5405.8 Fe I 15 5397.1 Fe I 15 5394.7 Mn I 1 3859.9 Fe I 4
52	3		6795	5436	4530	3883	5434.5 Fe I 15 5429.7 Fe I 15 5432.5 Mn I 1
53	2		6810	5448	4540	3891	5446.9 Fe I 15 5455.6 Fe I 15

Table VIII.

Line No.	Strength	Observed wavelength −3	−4	−5	−6	−7	Identifications
54	4		6855	5484	4570	3917	4571.1 Mg I 1
55	2		6882	5506	4588	3933	5501.5 Fe I 15 5506.8 Fe I 15 5497.5 Fe I 15 3933.7 Ca II 1
56	2		6945	5556	4630	3969	3961.5 Al I 1 3968.5 Ca II 1
57	2		6978	5582	4652	3987	5577.3 O I 3F
58	5		7370	5896	4913	4211	5890.0 Na I 1 5895.9 Na I 1
59	3		7395	5916	4930	4226	4226.7 Ca I 2
60	2		7445	5956	4963	4254	5956.7 Fe I 14 5949.3 Fe I 14 5958.2 Fe I 14
61	2		7570	6056	5047	4326	5041.8 Fe I 36
62	5		7665	6132	5110	4380	4375.9 Fe I 2 5110.4 Fe I 1

6. Temporal evolution of the afterglow spectrum

The decay of the individual spectral lines and continua was measured on the Ondřejov spectrum. The automatic gain control of the image intensifier of the BETSY spectrograph decreased the gain after the fireball brightening and the gain was slowly recovering during the afterglow radiation. The BETSY spectrum would therefore be difficult to use for photometric purposes. Moreover, the spectrograph has not been calibrated for spectral sensitivity in the high spectral orders.

The evolution of the intensity of the continuous radiation is shown in Figure 8. At the beginning, the intensity decreased rapidly. The decrease was followed by a standstill, pronounced especially in segment 1. Finally, a gradual exponential decrease occurred. The red and the yellow continuum behaved similarly. No big change of the shape of the continua during the decay was evident.

The measurement of the decay of the atomic lines was complicated by the fact that the intensity range of the video system is only 8 bits. Bright lines are saturated at the beginning and could be measured only after some time. Faint lines, on the other hand, are visible only at the beginning. Nevertheless, when in the measurable range, the decay of

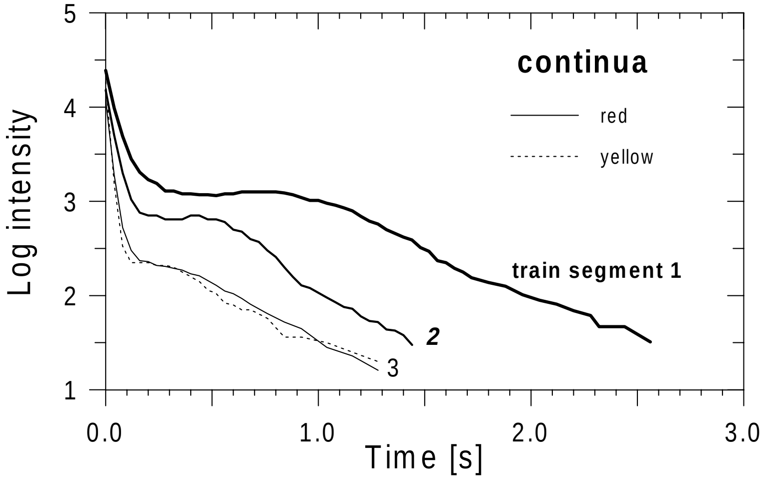

Figure 8. The decay of intensity of the continuous radiation in the afterglow spectrum during the first seconds. The intensity is given in relative units. The red continuum was measured at three train segments, the yellow continuum (dashed line) could be measured only on segment 3.

all lines could be fitted by a simple exponential function:

$$\log I = \log I_0 + Bt, \tag{1}$$

where I is the line intensity, t is time, I_0 is the intensity at time zero and B is the decay coefficient. The values of $\log I_0$ and B for all measured lines at three train segments are given in Table IX. The values of I_0 have been corrected for spectral sensitivity of the instrument. For each line, the time interval t_1,t_2 covered by the measurements is also given. Time zero corresponds to the train formation just after meteor passage at a given place. Note that lines 29, 41, and 42 could be measured at segment 1 only after they appeared in the field of view following the shift of the camera.

For most of lines in Table IX the data of the dominant atomic transition are given: the element, the excitation potential of the upper level, E_k, and $\log gf$, the oscillator strength multiplied by statistical weight of the lower level. These data are not given if there is no one dominant contributor to the observed line, or the line is too faint, or it does not belong to a neutral atom of meteoric origin (i.e. O I and Ca II excluded). Atomic data given in Table IX were used for further consideration of physical conditions in the train. Detailed identification of all lines is given in Table IV.

Lines no. 3, 5, 28, 29, 41, and 42 exhibit the slowest decay. All have low excitation potential not exceeding 2.5 eV. Figure 9 shows that there is a definite dependency of the decay rate on excitation potential.

Table IX.

No	El	E_k	log	segment 1				segment 2				segment 3			
		eV	gf	I_0	B	t_1	t_2								
1												4.03	-4.42	.00	.50
3	K	1.72	-0.17	5.07	-1.04	0.70	2.00	4.47	-1.79	.00	1.10	4.00	-2.44	.00	.80
4				4.93	-2.78	0.08	0.30								
5	Fe	2.43	-4.85	5.02	-1.45	0.08	0.50	4.72	-3.51	.00	0.30	4.05	-3.34	.00	.60
6	Mn	3.08	-0.13	6.66	-2.02	0.65	1.25	5.71	-3.52	.00	0.20	4.96	-4.45	.00	.45
7	Na	3.62	0.74	5.38	-3.25	0.08	0.30	4.95	-5.84	.00	0.20				
8				5.63	-5.37	0.08	0.30	5.07	-8.94	.00	0.16				
9				5.40	-2.67	0.08	0.50								
10	Fe	2.94	-3.35	6.62	-2.28	0.40	1.25	5.78	-3.03	.05	0.70	5.21	-4.11	.00	.70
11				6.48	-3.77	0.20	0.80	5.68	-5.09	.00	0.40	5.28	-10.4	.00	.20
12				6.06	-3.54	0.10	0.70								
13				6.11	-5.16	0.10	0.60								
14	Fe	2.83	-3.03	7.62	-2.68	0.80	1.80	6.90	-4.14	.40	1.00	5.63	-4.70	.00	.80
15	Fe	2.85	-2.92	7.44	-2.66	0.80	1.80	6.70	-4.11	.40	0.80	5.60	-4.60	.00	.65
16	Fe	2.87	-3.21	7.22	-2.63	0.70	1.70	6.57	-4.10	.40	0.80	5.43	-4.63	.00	.65
17	Fe	2.88	-3.50	6.94	-2.69	0.70	1.60	6.12	-4.00	.30	0.80	5.15	-4.70	.00	.65
18	Mg	2.71	-5.40	7.33	-2.61	0.80	1.80	6.41	-4.11	.40	0.90	4.96	-4.44	.00	.60
19	Cr	3.68	-0.50	4.69	-5.63	0.00	0.35								
20	Mg	6.98	-0.37	4.67	-11.1	0.00	0.18								
21	Fe	5.41	-0.41	4.71	-6.46	0.00	0.30	4.46	-13.9	.00	0.16				
22	Fe	5.39	0.04	4.65	-6.20	0.00	0.30	4.68	-15.6	.00	0.16				
23	Fe	5.35	0.20	4.75	-6.44	0.04	0.30	4.82	-14.1	.00	0.16				
24	Fe	5.31	0.32	4.86	-6.56	0.04	0.35	4.99	-14.2	.00	0.16				
25	Fe	3.33	-2.64	4.16	-1.72	0.15	0.80	4.57	-5.79	.00	0.36				
26	Fe	3.94	-2.20	4.63	-2.53	0.24	0.45	5.11	-5.56	.00	0.40	4.04	-5.44	.00	.25
28	Fe	2.43	-3.76	7.49	-1.84	1.20	2.15	7.26	-3.96	.60	1.20	5.57	-3.92	.00	.80
29	Fe	2.42	-3.77	6.78	-1.50	2.50	3.00	7.27	-3.95	.60	1.20	5.70	-3.99	.00	.80
30	Fe	2.47	-4.33					6.38	-4.09	.30	0.80	5.29	-4.92	.00	.50
31	Fe	2.48	-4.79					5.67	-3.84	.10	0.60	5.18	-6.02	.00	.40
32	Fe	2.47	-4.40					5.83	-3.72	.24	0.70	5.03	-5.10	.00	.40
33	Fe	3.21	-1.32					6.02	-4.41	.24	0.70	5.16	-5.52	.00	.40
34	Fe	3.24	-1.47					5.56	-4.66	.10	0.60	5.06	-6.67	.00	.40
35	Fe	3.27	-1.64									4.71	-6.97	.00	.40
36	Fe	3.28	-1.61									4.88	-6.25	.00	.40
37	Fe	3.24	-1.68									4.82	-6.60	.00	.40
40												5.20	-10.2	.00	.20
41	Na	2.10	0.29	5.56	-0.81	2.50	3.50					5.50	-3.45	.04	.90
42	Ca	1.89	-4.30	4.23	-0.63	2.50	3.50								

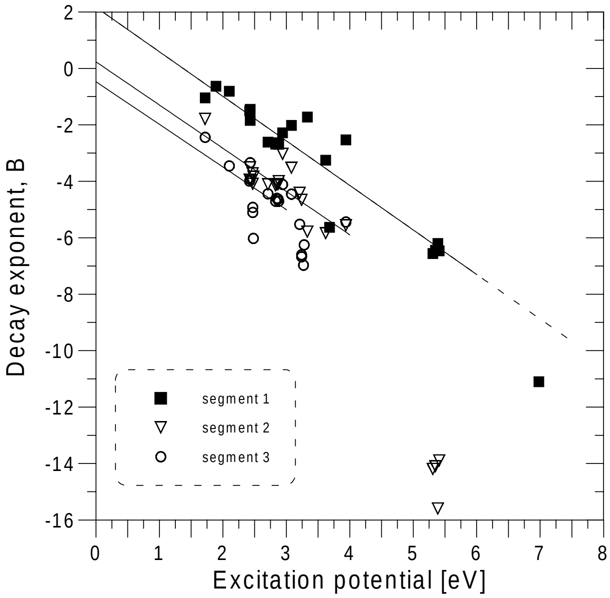

Figure 9. The dependency of the decay rate of lines of neutral atoms on their excitation potential.

Although the spread is relatively large, the decay rate of most lines is nearly proportional to the excitation potential:

$$B = B_0 + DE \tag{2}$$

The proportion constant is nearly the same for all segments: $D = -1.5\,\mathrm{s}^{-1}\mathrm{eV}^{-1}$. The constant B_0 (a decay rate of a fictive zero eV of excitation line) is, however, different. B_0 may indicate a change in abundance of atomic species, for example. For segments 2 and 3 B_0 is, within the limits of errors, nearly zero but for segment 1 it is about $2\,\mathrm{s}^{-1}$. Lines of the highest excitation do not follow Eq. (2) at all. They decay more quickly. Also the lines of Ca II and O I (not shown in Figure 9) decay more quickly.

The decay rate of the continuous radiation is slower than of most of lines. The asymptotic decays in Figure 8 correspond to the values of B from -1.0 to -1.2. The continuum decay is slightly slower at segment 1 and for the yellow continuum than for the red continuum.

7. Physical conditions in the afterglow

7.1. INITIAL CONDITIONS

In this section we will consider physical conditions during the first seconds of the formation of a persistent train at the time of the afterglow, in particular the gas temperature. We have at our disposal the data from Table IX which enable us to determine the intensities of all lines at one time instant. In the following simple approach, we assume that the train is optically thin. Then, the intensity of a line, I_{ki}, is directly proportional to the population of the corresponding upper level, N_k, (i.e. total number of atoms in the upper state in the whole train segment):

$$I_{ki} \sim A_{ki} N_k, \tag{3}$$

where A_{ki} is the radiative transition probability, which is directly related to the oscillator strength.

We assume statistical equilibrium, i.e. the number of downward and upward transitions at a given time is the same:

$$N_i(A_i + C_{i0}) = N_0 C_{0i}, \tag{4}$$

where $A_i = \sum_{j<i} A_{ij}$ is the total radiative deexcitation rate of the level i and C_{ij} are the collisional transitional probabilities. Index 0 designs the ground level. For simplicity, we consider only collisional transitions involving the ground level. The following relations for collisional transitions can be written (Mihalas 1978):

$$C_{0i} = \frac{g_i}{g_0} \mathrm{e}^{-E_i/kT} C_{i0} = b(T) C_{i0}, \tag{5}$$

$$C_{0i} = n_\mathrm{e} \mathrm{e}^{-E_i/kT} Q_{0i}(T) \tag{6}$$

where we designed the Boltzmann factor as $b(T)$. Here T is temperature, k is the Boltzmann constant, g are statistical weights of the levels, and n_e is the density of free electrons. Q_{0i} is a complicated function slightly dependent on temperature.

Combining the above equations and ignoring for simplicity the statistical weights, we arrive at the following order-of-magnitude relation for the level population:

$$\frac{N_i}{N_0} = \frac{b(T)}{\dfrac{A_i}{n_\mathrm{e} Q_i(T)} + 1} \tag{7}$$

The ratio $A_i/n_\mathrm{e} Q_i$ is important for a deviation of level population from the value in thermal equilibrium (TE). TE is satisfied as long as

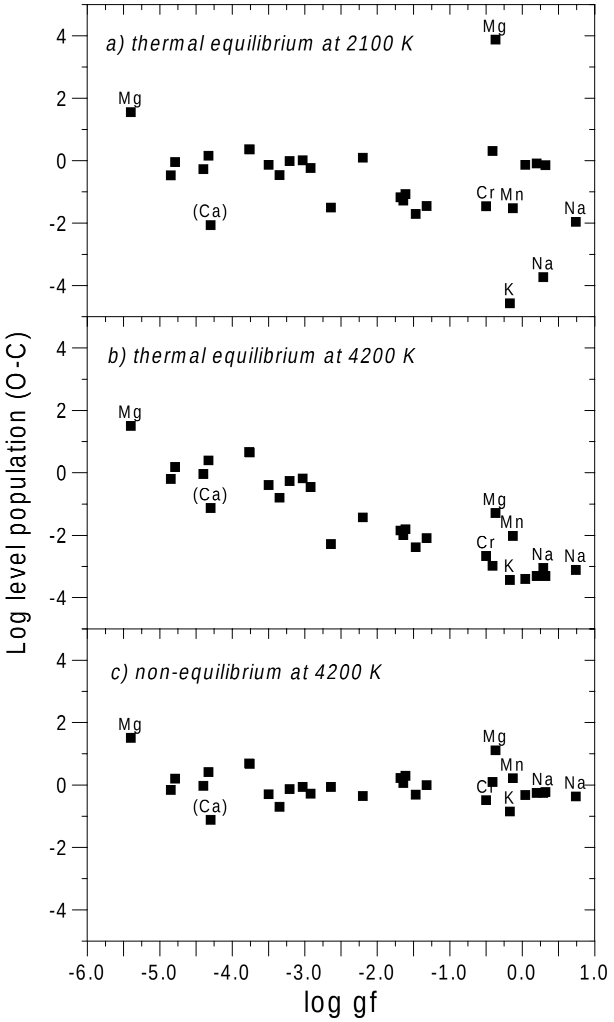

Figure 10. The difference $(O - C)$ of the logarithm of level population computed from the observed line intensity (Eq. 3) and for a given temperature and density (Eq. 7). Each point represents one line. Unmarked points belong to iron lines. The $(O-C)$ is given as a function of $\log gf$ of the line. Plot a) $T = 2100$ K and $n_e Q \gg A$ for all lines.; b) the same for $T = 4200$ K; c) $T = 4200$ K and $n_e Q = 10^5$ s^{-1}.

$A_i \ll n_e Q_i$. If electron density is low and collisions are infrequent, levels are depopulated by radiative transitions. The levels where a strong allowed transition originates are the most affected.

Using the data from Table IX, line intensities 0.1 s after the train formation (0.05 s for segment 3) were determined and the level populations were computed using Eq. (3). The results were then compared with predictions from Eq. (7). Two parameters were varied, temperature

T, which affects the Boltzmann factor $b(T)$, and the value of $n_e Q_i$, which was, for simplicity, taken the same for all lines and was assumed to be independent of temperature. To use all available data, all three train segments and all elements were combined. The level populations derived from segments 2 and 3 were risen by empirically determined factors of 0.5 and 1.4 in logarithmic scale, respectively, to be on the same scale with segment 1. Chondritic relative abundances of elements were assumed.

Figure 10a shows the observed minus predicted level populations as a function of the $\log gf$ of the corresponding line for a temperature of 2100 K and thermal equilibrium. This temperature fits many iron lines relatively well but some iron lines are underpopulated by and order of magnitude and, moreover, lines of other elements deviate by up to four orders of magnitude to both sides. When assuming a temperature of 4200 K (Figure 10b), the scatter of the $(O-C)$ values is substantially reduced. The $(O-C)$'s, however, do not lie near zero but form a clear dependence on $\log gf$. This suggests that the temperature is correct but the assumption of TE is not correct. Indeed, the assumption of $T = 4200$ K and $n_e Q = 10^5$ s^{-1} (Figure 10c) explains the population of most levels relatively well, considering all the simplifications we made. Only the two lines of Mg deviate. Magnesium seems to be overabundant in the train, for which we have no explanation. In the meteor itself the Mg abundance was normal. The line of Ca deviates a little bit as well, but this line was out of the field of view most of the time and was seen only after the camera movement, when it was already faint.

The average value of $n_e Q = 10^5$ means that radiative depopulation was really important for many levels. For the Na line, for example, the radiative deexcitation rate is $A = 6 \times 10^7$ s^{-1}. For the intercombination lines of Fe, Ca, and Mg, on the other hand, the A value is in the range 10^2 to 10^4 and the radiative deexcitation is not so important. These lines are therefore much brighter when compared to the allowed transitions than in laboratory conditions.

The relative enhancement of the intercombination lines has been observed earlier in the spectra of wakes of bright fireballs (Halliday 1968, Borovička & Spurný 1996). The mechanism of a low collisional rate is clearly the same. In this sense, the afterglow was like a "prolongated wake" The wake normally does not separate from the mother meteor and the radiation as a given point lasts for less than 0.1 s. Now it was observed for several seconds.

7.2. Temporal evolution

As mentioned earlier, we do not have enough data to derive the temperature independently at various time instants. Even the temperature derived in the previous section was obtained by extrapolation of line intensities and combining three train segments. We will continue in this approach and combine several simple equations to obtain the temperature trend.

It was found that the decay of line intensities depends on excitation potential, not on transition probability. The decay is therefore due primarily to the decrease of temperature, not density. The level populations N_i, total abundance of an atom N, and temperature T are functions of time and are connected by the Boltzmann equation (modified by a radiative deexcitation factor in some cases, which, however, is nearly constant and is not important here):

$$\log(N_i(t)) = \log(N(t)) - \frac{5040}{T(t)} E_i. \tag{8}$$

T is given in Kelvins, E in Electron Volts. The decay of line intensities and thus level populations could be fitted with an exponential function:

$$\log(N_i(t)) = \log(N_i(0)) + B_i t. \tag{9}$$

The decay rate was found to depend linearly on excitation potential for most lines:

$$B_i = B_0 + D E_i. \tag{10}$$

Substituting to Eq. (9) from (8) and (10) and comparing the coefficients with (8), we find the solution:

$$\log N(t) = \log N(0) + B_0 t \tag{11}$$

and

$$\frac{5040}{T(t)} = \frac{5040}{T(0)} - Dt \tag{12}$$

Equation (11) shows that the total number of atoms in segments 2 and 3, where $B_0 \approx 0$ (Figure 9), was nearly constant, while in segment 1, where $B_0 \approx 2$, the number of atoms increased with time. This is probably connected with a secondary ablation that may be induced by the movement of the whole segment (see Sect. 4). Both effects are further evidence that meteoric debris was left behind. Of course, these conclusions are valid only for the first second or few seconds, when the line decay was measured.

The value of the constant D in Eq. (12) was found to be nearly the same in all segments ($D \approx -1.5$), so the temperature decay was nearly

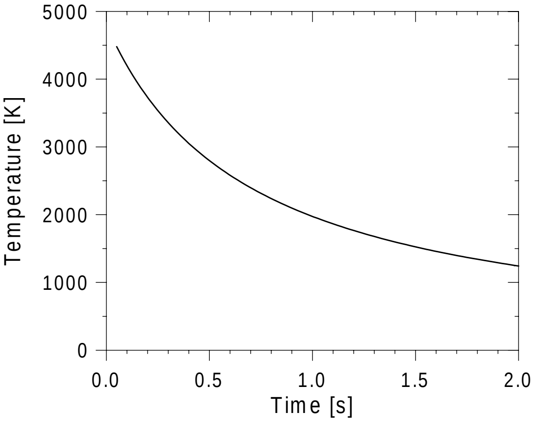

Figure 11. The temperature of the train during the first two seconds as derived from the atomic line intensities and their decay rates.

the same in the whole train. The function (12) is displayed in Figure 11. At the beginning, the train temperature nearly corresponded to the temperature of the main spectral component in the fireball spectrum, i.e. 4500–5000 K. Within one second, the temperature decreased to 2000 K and during the next second to 1200 K. We do not claim that the temperature strictly followed function (12) but Figure 11 gives a good idea on the temperature decay.

8. Persistent train emission

As explained in Sect. 5, the spectrum of the persistent train was captured in the first order at 37 seconds and from 1 minute and 23 seconds after the train formation. The spectrum at these times consisted only from continuous radiation as shown in Figures 6 and 12. The spectrum was virtually identical at both times and no spectral change occurred in the following minutes, either. The continuum only weakened.

The continuum extends from 5000 Å to at least 7500 Å with the maximum near 6200 Å and shows no significant structure. The spectral resolution is worse than for the afterglow because of the physical width of the train, nevertheless, it is still reasonable. The physical width of the train can be seen on the zero order image in the upper panel of Figure 12. Any atomic lines or molecular bands separated more than this width should be resolved, if they were present in the spectrum.

The continuum is probably identical with the yellow continuum observed in the initial stages of the train. In addition, the red continuum may also be present near 8000 Å but the sensitivity in this region is low and the signal is very noisy. The yellow continuum is very proba-

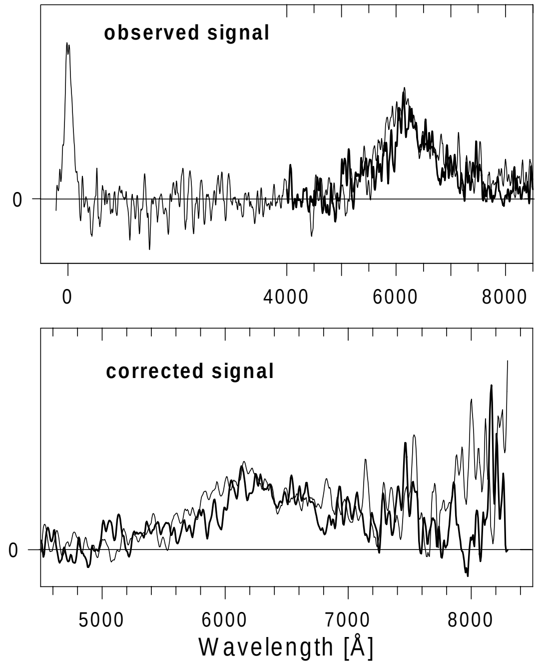

Figure 12. The spectrum of the train 37 s (bold line) and 85 s (thin line) after the train formation. The upper panel shows the uncorrected spectrum and the zero order. The lower panel shows the signal after correction to spectral sensitivity of the instrument.

bly due to molecular emissions but the source was not unambiguously identified. Various molecules like FeO, CaO, TiO, and CN have bands in this region but all should show structure under the given resolution. The most probable source seems to be the NO_2 molecule which has an extended featureless continuum and has been proposed as the possible source of the luminosity of persistent meteor trains (Rajchl 1975, Murad 2000). If NO_2 is really the source, then the energy for the radiation comes from the chemical reaction as proposed by Rajchl (1975) and Murad (2000):

$$NO + O \rightarrow NO_2^* \rightarrow NO_2 + h\nu .$$

According to Murad (2000), the reaction proceeds on the surface of metallic dust grains.

9. Comparison with other data

There are not many meteor train spectra in the literature. Nasirova and Nasirov (1966) presented a photographic spectrum of a Leonid meteor train taken in 1965. Most of the radiation was due to a continuous radiation between 5200–6400 Å, though some lines were present as well. This spectrum is the most similar to our spectrum at later times. Other good photographic spectra were taken by Abe *et al.* (2000) and Borovička *et al.* (1996). Both spectra show the Na I line but also a number of other atomic lines which differ from our spectrum. The brightest line of the Leonid train spectrum taken by Abe *et al.* (2000) 12–22 s after the train formation is the Mg I line at 5180 Å, which in our spectrum is totally overwhelmed by the Fe I 1 lines. The Fe I multiplets 1, 2, and 3 were not found in Abe's spectrum though the intercombination line Mg I 1 at 4571 Å is quite bright. The Perseid train spectra taken in Japan (Rajchl *et al.* 1995) also contain the Mg I 5180 Å line and not the Fe I 5110 Å line.

Borovička *et al.* (1996) identified the forbidden nebular lines of O I, O II, O III and S II, in the spectra of Perseid trains taken 5–25 s after the train formation. Since a prism spectrograph was used, the identifications may be questionable. Nevertheless, it seems that the differences between different authors are not largely due to inaccurate interpretation. Train spectra may really differ according to the altitude, density, age and other parameters of the train.

Zinn *et al.* (1999) reported that a Leonid meteor train was visible for over an hour on an all-sky imager with a Na 5890 Å filter. This, however, does not mean that sodium was the emitter. The signal could well be caused by the yellow continuum. Zinn *et al.* (1999) also presented a model and concluded that the persistent train emission should be done by the O I 5577 Å airglow with additional contributions from Na I and from NO_2 chemiluminescence.

Numerous color pictures of meteor trains were presented on the internet and in astronomical journals following the 1998 and 1999 Leonids. Many trains show a dominant yellow-orange color which may be due to the yellow continuum. There are, however, also fainter sections which show a distinct blue or red color, suggesting that train spectra may vary also within one persistent train.

10. Summary

In conclusion, we presented here for the first time resolved spectroscopy of a persistent meteor train. The number of observed spectral lines was larger than ever detected in a meteor train. The temperature of the train in the first seconds of its existence was derived. For the first time, the spectrum of the persistent train was also recorded tens of seconds and minutes after the train formation. At that time, the luminosity was done by a yellow continuum.

The facts from the previous sections can be summarized as follows: The fireball reached about -13 mag at a relatively low altitude between about 85 and 80 km. The whole trajectory extended from as high as ≥ 190 km to a very low end for a Leonid, 56 km. At its peak, the fireball spectrum contained relatively bright H lines and the inferred hydrogen abundance is about three times higher than in Perseid fireballs. The lines in the fireball spectrum can be divided into several groups according to their origin (atmospheric or meteoric) and the degree of excitation. The relative brightness of the groups of lines changed with time, in dependence on the ablation rate.

A bright afterglow was formed at the position of bright fireball flares at a relatively low altitude, 85–75 km. The afterglow decayed quickly over a period of a few seconds and a persistent train remained visible for at least eleven minutes. The afterglow emission originates from atomic compounds ablated by the meteor as well as from excited atmospheric gas. We also find evidence for continuum emission of dust at temperatures around the evaporation temperature of silicates ($\approx$1400 K), which is likely meteoric debris that has not fully ablated. Part of the train had its own inertia and moved downward for a second, providing additional energy for radiation and ablation.

The upper part of the train was stretching up to the altitude of 140 km and was caused by the forbidden 5577 Å oxygen line which has a long radiative lifetime. This emission is not related to that caused by the ablation matter.

After the formation of the train, the temperature of the gas was the same as the temperature of the main part of the ablated gas in the fireball itself, i.e. 4500–5000 K. The temperature then decreased rapidly, causing a brief initial decrease of the train luminosity. The (electron) density in the train was low and thermal equilibrium was not satisfied in the train. Radiative deexcitation of atomic levels was important and semi-forbidden lines were enhanced relatively to the allowed transitions. The apparently high Mg/Fe ratio in the train was not explained. In the fireball itself the Mg/Fe ratio was normal.

After about 30 s or less, the glow ceased and a persistent train was observed having a featureless continuum, possibly due to NO_2. The prevalence of this emission may be associated with the presence of dust. The comparison with other data suggest that other trains may show different emissions and different structure. There may be various kinds of meteor trains which differ by their altitude, density, dust to gas ratio, and ongoing chemistry. More observations are needed to reveal all possible mechanisms responsible for meteor train phenomenon. Better resolution is needed to reveal the true nature of continuous and quasi-continuous emissions.

Acknowledgements

The 1999 Leonid Multi-Instrument Aircraft Campaign was made possible by grants from the NASA Exobiology, Planetary Astronomy, and Astrobiology Advanced Missions and Technology Programs, NASA Ames Research Center, and the U.S. Air Force. The data analysis was supported by grant 205/99/0146 from the Grant Agency of the Czech Republic. *Editorial handling:* Frans Rietmeijer.

References

Abe, S., Ebizuka, N., Watanabe, J., Murayama, H., and Ohtsuka, K.: 2000, *Meteorit. Planet. Sci.*, in press.

Borovička, J.: 1994, *Planet. Sp. Sci.* **42,** 145–150.

Borovička, J. and Betlem, H.: 1997, *Planet. Sp. Sci.* **45,** 563–575.

Borovička, J. and Boček, J.: 1995, *Earth, Moon, Planets* **71,** 237–244.

Borovicka, J. and Majden, E.P.: 1998, *J. R. Astron. Soc. Canada* **92,** 153–156.

Borovicka, J. and Spurný, P.: 1996, *Icarus* **121**, 484–510.

Borovička, J., Zimnikoval, P., Škvarka, J., Rajchl, J., and Spurný, P.: 1996, *Astron. Astrophys.* **306**, 995–998.

Halliday, I.: 1961, *Publ. Dominion Obs. Ottawa* **25**, 3–16.

Halliday, I.: 1968, in Ĺ. Kresák and P.M. Millman (eds.), *Physics and Dynamics of Meteors,* IAU Symp. 33, D. Reidel Publ. Co., Dordrecht, pp. 91–104.

Jenniskens, P. Butow, S., and M. Fonda: 2000, *Earth, Moon, Planets* **82**–**83**, 1-26.

Jenniskens, P. and Rairden, R.: 2000, *Earth, Moon and Planets* **82-83**, 459–472.

Mihalas, D.: 1978, *Stellar Atmospheres,* W.H. Freeman and Co, San Francisco, 650 pp.

Millman, P.M.: 1953, *Nature* **172,** 853.

Moore, C.E.: 1945, *A multiplet table of astrophysical interest*, Contr. Princeton Obs. **20**.

Murad, E.: 2000, *Heterogeneous chemical processes as source of persistent meteor trains*, in preparation.

Nasirova, L.I. and Nasirov, G.A.: 1966, *Astron. Tsirk.* **370,** 1–2.

Rajchl, J.: 1975, *Bull. Astron. Insts. Czech.* **26,** 282–288.

Rajchl, J., Boček, J., Očenáš, D., Škvarka, J., Zimnikoval, P., Murayama, H., and Ohtsuka, K.: 1995, *Earth, Moon, Planets* **68,** 479–486.

Spurný, P., Betlem, H., van't Leven, J., and Jenniskens, P.: 2000a, *Meteorit. Planet. Sci.* **35,** 243–249.

Spurný, P., Betlem, H., Jobse, K., Koten, P., and van't Leven, J.: 2000b, *Meteorit. Planet. Sci.* **35,** in press.

Zinn, J., Wren, J., Whitaker, R., Szymanski, J., ReVelle, D.O., *et al.*: 1999, *Meteorit. Planet. Sci.* **34**, 1007–1015.